Comparison of Hypersonic Experiments and PNS Predictions Part I: Aerothermodynamics

Bilal A. Bhutta* and Clark H. Lewis†
VRA, Inc., Blacksburg, Virginia 24063

A parabolized Navier-Stokes (PNS) scheme has been developed to study perfect-gas and equilibrium-air hypersonic flows around three-dimensional configurations. This numerical scheme is unconditionally time-like in the subsonic as well as the supersonic flow regions and does not require any sublayer approximation. This three-dimensional PNS scheme has been used to predict hypersonic flowfields over various blunt conical configurations under either flight or wind-tunnel conditions. The test cases cover a Mach number range of 6.9–20 and an angle-of-attack range from zero to 27 deg. The resulting predictions of wall heat-transfer rate are compared with flight or experimental wind-tunnel data and are found to be in excellent agreement under laminar and fully turbulent conditions. The predictions of the transition model of Dhawan-Narasimha, however, significantly differ from the observed flight data. Numerical results for large angle-of-attack conditions show that accurate modeling of the leeward crossflow separated region is essential for accurately predicting the associated leeward wall heating rates.

Nomenclature

ALPHA = angle of attack with respect to forecone axis α, deg
DXMAX = maximum axial step size
h = static enthalpy
k = thermal conductivity
K = grid index in the ξ_3 direction
L = reference length for force and moment coefficients, also grid index in the ξ_2 direction
M = Mach number
n = iteration number
P,p = static pressure
PHI = circumferential angle ϕ, deg
Pr = Prandtl number
QW = wall heat-transfer rate, BTU/ft^2-s
Re = Reynolds number, $(\rho VRn)/\mu$
RN,Rn = nose radius
T = static temperature
u = x component of local velocity
V = total velocity
v = y component of local velocity
w = z component of local velocity
X,x = coordinate along body axis
y = y coordinate
z = z coordinate
α = angle of attack with respect to forecone axis, deg
ϵ = M_∞/Re_∞
μ = viscosity
ξ_1 = marching or streamwise coordinate
ξ_2 = coordinate measured from the body to the outer bow shock
ξ_3 = coordinate measured from the windward to the leeward pitch plane
ρ = static density
ϕ = circumferential angle measured from the windward side, deg
γ = ratio of specific heats

Subscripts

, = partial derivative
∞ = freestream quantity
w = wall quantity
0 = total conditions
k = indicial notation representing 1, 2, and 3

Superscripts

n = index for iteration
j = index in ξ_1 direction

Introduction

THE existing numerical schemes for predicting hypersonic external flows over three-dimensional geometries consists of Navier-Stokes (NS), parabolized Navier-Stokes (PNS), and viscous shock-layer (VSL) schemes. The NS schemes[1-3] are typically very time consuming and not well suited for various parametric studies required for design and analysis purposes. On the other hand, the existing VSL schemes[4-6] have a basic limitation of being parabolic in the crossflow direction and, consequently, cannot march through crossflow separated regions. However, even under these conditions, the flowfield in the nose region is attached, and the VSL schemes represent an accurate and efficient way of generating the nose solutions for starting other (more accurate) afterbody methods that can treat crossflow separation (such as the PNS schemes).

One of the objectives of this paper is to demonstrate the accuracy, robustness, and computational efficiency of a three-dimensional PNS scheme capable of treating perfect-gas and equilibrium-air hypersonic flows over complex three-dimensional configurations at large angles of attack (up to 27 deg). The axisymmetric version of this PNS scheme was first presented by us in 1985.[7] The present three-dimensional PNS scheme is a result of continuous development of this PNS scheme since that time.[8-14] This three-dimensional PNS scheme uses a general curvilinear coordinate system and does not require any sublayer approximation.[9] Recently, this unconditional time-like nature of our basic PNS scheme was further demonstrated by extending it to the hypersonic blunt-body region and unconditionally marching it through the subsonic blunt-body region.[10] All other three-dimensional PNS schemes[15-21] being used in the CFD community use some sort of a sublayer approximation to keep the numerical solutions stable in the near-wall subsonic flow region. These sublayer

Presented as Paper 90-3068 at the AIAA 8th Applied Aerodynamics Conference, Portland, OR, Aug. 20-22, 1990; received Nov. 15, 1990; revision received Feb. 11, 1991; accepted for publication Feb. 12, 1991.

*Chief Scientist. Senior Member AIAA.
†President. Associate Fellow AIAA.

models represent a substantial approximation in the way the near-wall subsonic sublayer region is treated and, thus, limit the numerical solution accuracy. In many cases these numerical inaccuracies represent severe limitations on the computational grids that can be used. The present three-dimensional PNS scheme not only provides enhanced solution accuracy by not requiring any sublayer approximation but also is robust enough to provide stable and accurate solutions over a wide range of coarse-to-fine grids.

In this paper we have used our three-dimensional PNS scheme over a wide range of Mach number and angle-of-attack conditions. Various blunt conical configurations have been studied under wind-tunnel or flight conditions. Comparisons have been made with available flight or experimental wind-tunnel data on wall heat-transfer distributions. A wide range of coarse-to-fine grids have been used to demonstrate the accuracy and robustness of this three-dimensional PNS scheme. In general, the results show that the predictions of the present three-dimensional PNS scheme are in excellent agreement with available data.

Solution Scheme

Numerical Formulation

The coordinate system used for the present three-dimensional PNS scheme is a general curvilinear coordinate system (ξ_1,ξ_2,ξ_3). Also, a body-fixed orthogonal (Cartesian) coordinate system is chosen such that the origin of the Cartesian coordinate system is at the tip of the blunt nose, and the x axis is aligned with the axis of the body. The flowfield unknowns are chosen to be ρ, ρu, ρv, ρw, T, and p.

Following the approach of Viviand[22] and Peyret and Viviand,[23] it can be shown that the three-dimensional full PNS equations can be written in the following vectorial form[7-14]:

$$f_{k,\xi_k} - \epsilon(s_{2,\xi_2} - s_{3,\xi_3}) = h \tag{1}$$

The first five equations of this vectorial set represent the differential conservation of mass, momentum, and energy, and the last (sixth) equation of this vectorial set is the algebraic equation of state for the gas mixture. For a perfect-gas model as well as an equilibrium-air gas model, this equation of state can be written in a nondimensional form as

$$\gamma_\infty p - Z^* \rho T = 0 \tag{2}$$

where $Z^* = 1$ for a perfect gas model and $Z^* = Z^*(p,T)$ for a equilibrium-air gas model.

By expanding these governing equations around the previous (nth) iteration,[7-14] using two-point streamwise differencing and solution under-relaxation,[11-14] we can write Eq. (1) as a block-pentadiagonal system of equations[11-14] that is solved using a pseudo-unsteady approach.[7-14] The final PNS equations are elliptic in the ξ_2 and ξ_3 directions. Therefore, in the present approach, central-differenced approximations are used for all ξ_2 and ξ_3 derivatives. However, the use of central-differenced schemes is typically associated with solution oscillations[7-14,17-20] and, thus, additional fourth-order dissipation terms are introduced in the ξ_2 (axis-normal) and crossflow (ξ_3) directions.[13,14] The accuracy of this smoothing formulation is further enhanced by restricting the axis-normal smoothing effects to only the pressure field.[11-14] In this manner, the axis-normal smoothing effects do not degrade the wall heat-transfer and skin-friction predictions.

Now a simple first-order accurate finite-difference representation of the streamwise convective flux derivatives (f_{1,ξ_1}) has no inherent mechanism to check or suppress the onset of streamwise numerical oscillations. The numerical filtering provided by this first-order backward-differenced approximation is proportional to the streamwise step size. As the streamwise step size decreases, the numerics become more and more sensitive to the high-frequency (small wave length) streamwise oscillations. To damp and suppress the growth of any streamwise solution oscillation, small amounts of second-order streamwise numerical dissipation effects are added to the first-order accurate streamwise convective derivatives such that in the limit of $\Delta\xi_1 \to 0$ the streamwise convective derivatives are continuous. This approach is based on a very simple damping model, and the streamwise diffusion effects in the convective streamwise derivatives are of the form

$$(f_{1,\xi_1})^{j+1} \cong (f_{1,\xi_1})_b^{j+1} - \theta f_{1,\xi_1\xi_1}\Delta\xi_1 \tag{3}$$

where the subscript b represents a first-order backward-differenced approximation. The second-order derivative to be used in Eq. (3) is estimated using a one-sided backward-differenced approximation. The appropriate values of θ appearing in the above damping model are between zero and unity. The lower limit of $\theta = 0$ is quite evident as it corresponds to the damping-free limit. The upper limit of $\theta \to 1$ corresponds to the limiting case of a vanishingly small stepsize ($\Delta\xi_1 \to 0$) and the requirement that the streamwise flux derivatives at the j and $j+1$ steps be continuous; i.e., $(f_{1,\xi_1})^{j+1} \to (f_{1,\xi_1})^j$. In the present approach, a simple linear model is used for θ such that $\theta \to 1$ as $\Delta\xi_1 \to 0$ and $\theta \to 0$ when $\Delta\xi_1$ is adequately large ($\Delta\xi_1 \geq \overline{\Delta\xi_1}$). Thus, the numerical accuracy of a large step-size solution is not compromised. Numerical tests show that, in general, $\overline{\Delta\xi_1}$ can be adequately approximated as 10% of the local shock-standoff distance.

For the perfect-gas model the mixture viscosity is obtained using the Sutherland formula,[24] and the specific-heat ratio is assumed to be a constant (1.4 for air). The mixture Prandtl number is also assumed fixed (0.72 for air), and the mixture thermal conductivity is obtained from the definition of mixture Prandtl number. In the case of equilibrium chemically reacting air, the mixture thermodynamic and transport properties are provided in the form of a table. The thermodynamic properties involve the mixture enthalpy $h(p,T)$ and mixture density $\rho(p,T)$ data and are based on the tabular data of Miner et al.[25] For the present calculations two different sets of these equilibrium-air transport property data were used. The first set of transport property data is based on the viscosity and thermal conductivity data developed by Peng and Pindroh.[26] The Prandtl number data were developed using these viscosity and thermal conductivity data and the mixture specific-heat data obtained by numerically differentiating the enthalpy data of Miner et al.[25] Additional details on the limits of these tabular data are given in Ref. 11. The other set of equilibrium-air transport property data uses the equilibrium-air composition of Miner et al.[25] along with the species viscosity curvefits of Blottner et al.[27] and Wilke's mixture formula[27] to determine the mixture viscosity of the equilibrium-air mixture. The thermal conductivity and Prandtl number data used are based on the data of Hansen.[28] For this reason this set of transport property data will be referred to as the Blottner-Hansen combination.

The initial conditions to start the PNS solutions were obtained from appropriate VSL blunt-body solution schemes.[4] The boundary conditions at the wall consist of the equation of state for the gas, no-slip boundary conditions, specified wall-temperature distribution, and zero pressure derivative in the ξ_2 direction ($p_{,\xi_2} = 0$).[7-14] The boundary conditions at the outer bow shock involve a fully implicit and crossflow-coupled shock-fitting approach, and the bow shock location is simultaneously predicted as the solution marches down the body.[11-14]

The crossflow boundary conditions consist of either 1) pitch plane-of-symmetry boundary conditions or 2) periodic boundary conditions for flows that do not have a pitch plane of symmetry. For cases with a pitch plane of symmetry, second-order accurate reflective or symmetric boundary conditions[20-21] are used in the pitch plane.

To properly treat the effects of strong crossflow solution-coupling effects, we have used a predictor-corrector solution approach[11-14] to solve the final block-pentadiagonal system of equations. This predictor-corrector scheme is divided into

three different steps[11-14]: 1) the predictor step, 2) the shock solution, and 3) the corrector step. In the predictor step, the implicit crossflow (ξ_3) coupling effects are neglected in favor of the axis-normal (ξ_2) coupling effects.[11-14] The crossflow-coupled implicit shock-fitting scheme[11-14] uses the results of the predictor step to predict the bow shock shape. The corrector step then uses the results of predictor and shock-fitting steps to reduce the overall pentadiagonal system of equations to a tridiagonal system in the crossflow direction.[11-14] This tri-diagonal system of equations is then solved using either plane-of-symmetry or periodic boundary conditions.

Grid Generation and Related Considerations

In our previous studies we have developed several grid generation schemes to better model complex three-dimensional configurations.[11-14] Recently we have also developed and used a new elliptic grid-generation scheme that is robust enough to model various complex as well as simple three-dimensional configurations in a fast and efficient manner. Thus, for any griding application with the present three-dimensional PNS scheme, we either use 1) a cylindrical grid or 2) an elliptic grid.

Cylindrical Grid Generation

A cylindrical grid-generation scheme is used for axisymmetric cross sections. In this cylindrical grid-generation scheme, equally spaced radial grids are generated in an axis-normal plane using a simple algebraic grid-distribution function. This is the simplest and the fastest grid-generation algorithm.

Elliptic Grid Generation

The elliptic grid-generation scheme used in this study is based on the work of Sorenson and Steger,[30] Chaussee and Steger,[31] and Kaul and Chaussee.[32] In this approach, a grid is generated between the body and the outer bow shock, which corresponds to the solution of two elliptic partial differential equations involving two forcing functions [$P(\xi_2, \xi_3)$ and $Q(\xi_2,\xi_3)$] that control the inclination and clustering of the grid. In the present approach, the forcing functions at the wall and at the shock boundaries are based on imposing grid orthogonality constraints, whereas inside they are exponentially varied from their specified values at the wall to the specified values at the shock. Currently this exponential variation is more rapid near the wall than at the shock. With this biasing, the grids generated have a more clustered appearance in the near-wall region.

Numerically it is very difficult to exactly satisfy the user-specified grid-clustering distribution and also simultaneously satisfy the orthogonality constraints of the elliptic grid (described by the P and Q functions between the wall and shock). The exponential variations of these forcing functions work very well, except that the grid generated does not correspond to the grid clustering finally required. However, one can use this grid and interpolate on it along ξ_3 = const lines to obtain the desired clustering. Unlike the actual grid before interpolation, the final interpolated grid is not exactly orthogonal everywhere. However, it does ensure grid orthogonality at the body and the shock and also ensures that the grid lines thus generated will never cross. In short, the basic requirements for a good computational grid are satisfied.

Since the final grid is generated by interpolating on the elliptic grid in the ξ_2 direction, the elliptic grid can be generated using fewer grid points in the ξ_2 direction. Furthermore, since exact orthogonality of the grid it not really needed, there is no additional advantage in driving the grid iterations to complete convergence. Thus, we use a maximum of 30 equally-spaced ξ_2 grid points for the elliptic solution and limit the number of grid iterations to 25. Typically, in these iterations the grid coordinates are converged to within 0.01–0.1% of their local value, and the residual norm has decreased by three orders of magnitude. In addition, in our scheme the full elliptic grid generation is done only once at a marching step, which is during the first solution iteration. In subsequent solution iterations at a step, only the shock points move along ξ_3 = const grid lines. Thus, during each iteration the elliptic grid between the body and the shock is not changed and only the grid points at the shock are adjusted to account for the shock motion. The required flowfield grid is generated by simply interpolating on this adjusted elliptic grid. This approach accounts for substantial computational savings, while retaining the powers of a full elliptic grid generation.

Transitional/Turbulent Flow Modeling

For turbulent flow calculations, we use a simple two-layer eddy-viscosity model consisting of an inner law based upon Prandtl's mixing-length concept and an outer law based on the Clauser-Klebanoff expressions. This model (introduced originally by Cebeci and Smith[33]) assumes that the inner law is applicable from the wall outward to the location where the eddy viscosity given by the inner law is equal to that of the outer law. The outer law is then assumed applicable for the remainder of the viscous layer. It is noted that the eddy viscosity degenerates to approximately zero in the inviscid portion of the shock layer. For this two-layer eddy-viscosity model, the turbulent Prandtl number is assumed to be 0.9 and, under cold-wall conditions, the boundary-layer thickness is calculated using a total enthalpy model. In this total enthalpy model, it is assumed that an appropriate value for the boundary-layer thickness is equal to the value of the normal coordinate where $[h_0 - h_w]/[(h_0)_\infty - h_w] = 0.995$.

For the transitional region, the present scheme uses the model proposed by Dhawan and Narasimha.[34] In this model, continuous transition is affected by defining a streamwise transition intermittency factor (γ_{tr}) that modifies the eddy viscosity over the transition region ($x \geq x_{tr}$). In this transition region ($x \geq x_{tr}$) the streamwise intermittency factor (γ_{tr}) is evaluated using the following relation:

$$\gamma_{tr} = [1 - \exp(-0.412\bar{x}^2)] \leq 1 \tag{4}$$

where $\bar{x} = 2.96(x - x_{tr})/x_{tr}$. The various coefficients and parameters used in this transition model are based on numerical tests and comparisons with experimental data.

Results and Discussion

The following sections show comparisons of the predicted wall heat-transfer rate with available flight or wind-tunnel data. In particular, comparisons have been made with the wall heat-transfer data from the Reentry-F flight vehicle[35] under laminar and transitional/turbulent conditions. Comparisons have also been made with the wall heat-transfer data from the NASA Langley Expansion Tunnel on a 12.84/7-deg bicone with/without a 7-deg nose bend.[36] The freestream conditions for these cases are summarized in Table 1. In general, these PNS calculations cover a Mach number range of 6.9–20

Table 1 Freestream conditions

Quantity	Cases			
	1	2	3	4–7
W-T/flight[a]	Flight	Flight	Flight	W-T
Mach number	19.25	19.97	19.97	6.89
Altitude, thousands of ft	120.0	80.00	65.00	—
Pressure, psf	9.585	58.56	119.6	45.57
Temperature, °R	435.6	395.1	388.9	2887.2
Angle-of-attack range, deg	0.0	0.14	0.715	0.0–27.0
Wall-temperature range, °R	650-860	775-1086	938-1331	545–700
Gas model	EQ[b]	EQ	EQ	EQ
Flow type	LAM[c]	TRNS[d]	TRNS	LAM
Nose radius, in.	0.114	0.140	0.151	0.151

[a]W-T = wind-tunnel conditions, flight = flight conditions.
[b]EQ = equilibrium-air gas model.
[c]LAM = laminar flow conditions.
[d]TRNS = transitional/turbulent flow conditions.

and an effective angle-of-attack range of 0–27 deg (see Table 1), where the effective angle of attack is defined with respect to the forebody axis. It should be noted that the computational grids used for all these PNS calculations use a near-wall grid spacing of 1.0×10^{-3}% of the local shock standoff distance. Numerical experience has shown such a fine grid spacing to be adequate for resolving the near-wall temperature and velocity gradients. The present three-dimensional PNS scheme is also stable and accurate over a wide range of small to large marching step-size (DXMAX). Typically, the afterbody PNS solutions are started at the sphere-cone tangent point with a small axial step-size, which is gradually increased to DXMAX in the afterbody region. As mentioned before, the initial conditions to start these PNS solutions were obtained from appropriate VSL blunt-body solution schemes.[4]

5-Deg Sphere-Cone (Reentry-F) Calculations

The data[35] from the Reentry-F flight experiment (1968) have been recently made available. This flight experiment involved the accurate measurement of surface heating rates on a long slender conical RV under laminar, transitional, and turbulent flow conditions. The particular RV consisted of a 5-deg half-angle sphere-cone with an overall length of 13 ft and an initial nose radius of 0.1 in.

Thompson et al.[37] have also used these data to make some comparisons with results obtained using a VSL scheme. Some of their comparisons were, however, limited due to the numerical difficulties encountered on the leeside by the VSL scheme when applied to long slender configurations even under relatively small angle-of-attack conditions.[37] This is primarily because the VSL solution scheme by its very nature is very sensitive to the accuracy of the input shock shape data, and it is numerically quite challenging to maintain the required accuracy for long slender configurations where the shock standoff distance is large and grows rapidly in the streamwise direction. The present three-dimensional PNS scheme is a higher order formulation that is more accurate and more stable and is not subject to these limitations.

Laminar Flow Conditions (Case 1)

The case 1 laminar conditions considered correspond to the Reentry-F flight altitude of 120,000 ft and zero angle-of-attack conditions.[35,37] The Mach number at this altitude is 19.25 and the nose radius (Rn) is 0.114 in. The numerical calculations were done using an equilibrium-air gas model. The effects of equilibrium-air transport property data based on the Peng and Pindroh data[26] and the Blottner et al.[27]/Hansen[28] combination are shown in Fig. 1, along with the corresponding flight data. These results show that under these conditions the particular choice of the transport property data does not have any identifiable effect on the predicted surface heating rate. Since the Blottner-Hansen data are valid over a much larger altitude range, we used these data for the remaining Reentry-F calculations.

In an effort to establish the appropriate grid size, the effects of axial and axis-normal grid refinement are shown in Figs. 2 and 3. Figure 2 shows the wall heat-transfer predictions using 50, 100, and 150 points in the axis-normal (body-to-shock) direction and DXMAX = 1Rn. This figure shows that the predictions of the 100- and 150-point grids are almost indistinguishable and, for the most part, are within a few percent of the flight data. The predictions of the 50-point grid are only 2–5% lower and also agree well with the data. The effects of axial grid refinement are shown in Fig. 3 and include the predictions of the 50-point grid using DXMAX of 0.15Rn, 1Rn, and 10Rn. The results show that even when the maximum

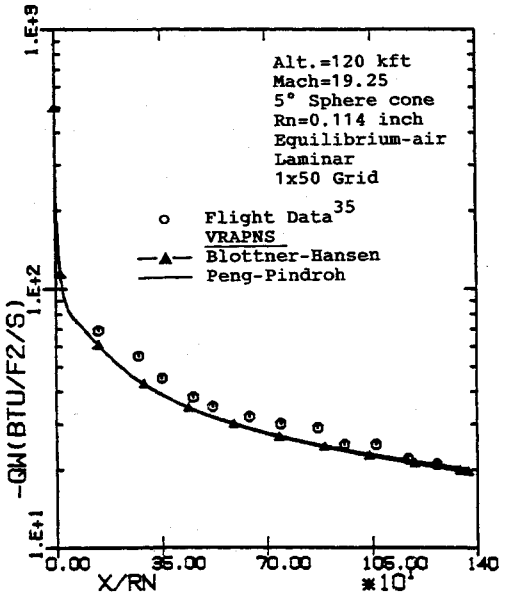

Fig. 1 Effects of equilibrium-air property data on the axial distribution of the wall heat-transfer rate for case 1.

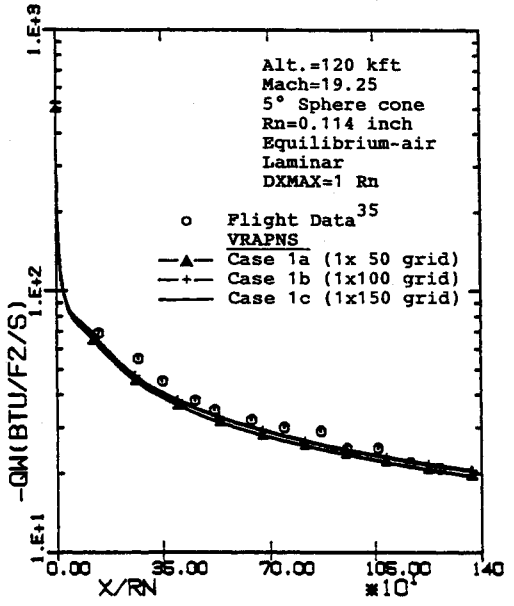

Fig. 2 Effects of axis-normal grid refinement on the axial distribution of the wall heat-transfer rate for case 1.

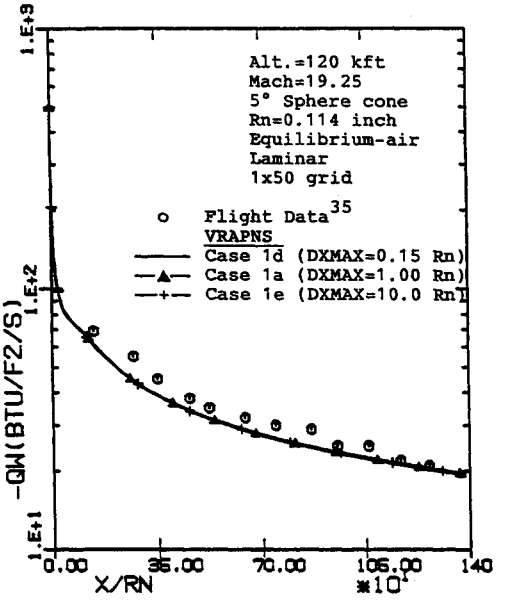

Fig. 3 Effects of axial grid refinement on the axial distribution of the wall heat-transfer rate for case 1.

Table 2 Computing times for equilibrium-air cases 1-3

Case	Altitude, thousands of ft	Mach no.	Flow type[a]	AOA, deg[b]	DXMAX, *Rn*	Grid[c] N3 × N2 × N1	Time, s[d]
1a	120	19.25	LAM	0.0	1.0	1 × 50 × 1384 C	87
1b	120	19.25	LAM	0.0	1.0	1 × 100 × 1384 C	296
1c	120	19.25	LAM	0.0	1.0	1 × 150 × 1384 C	498
1d	120	19.25	LAM	0.0	0.15	1 × 50 × 9116 C	513
1e	120	19.25	LAM	0.0	10.	1 × 50 × 177 C	16
2a	80	19.97	TRNS	0.14	2.5	9 × 100 × 474 C	269
2b	80	19.97	TRNS	0.14	2.5	9 × 100 × 474 C	289
3	65	19.97	TRNS	0.715	2.5	9 × 100 × 439 C	249

[a]LAM = laminar flow, TRNS = transitional/turbulent flow conditions.
[b]AOA = angle of attack.
[c]N1, N2, and N3 are the number of grid points in the streamwise, axis-normal, and crossflow directions, respectively. The notations of C means cylindrical grid.
[d]Computing times on Cray Y/MP with CFT77 compiler and autovectorization.

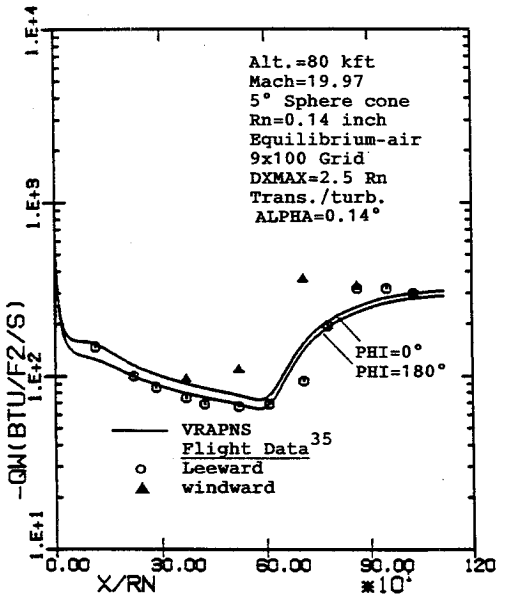

Fig. 4 Axial distribution of the wall heat-transfer rate for case 2 with Dhawan-Narasimha transition model.

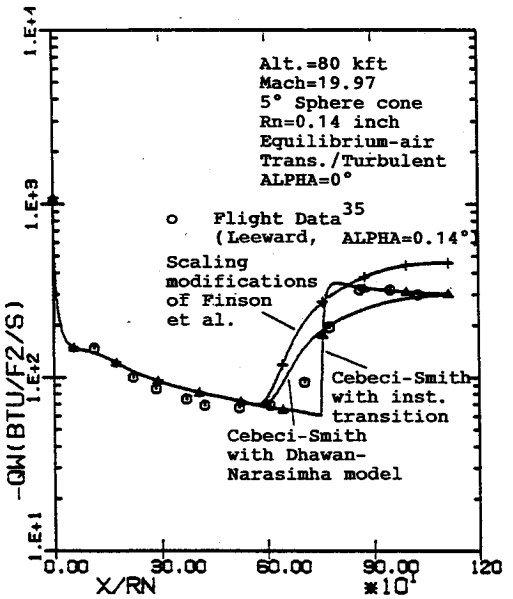

Fig. 5 Effects of transition/turbulent flow models on the axial distribution of the wall heat-transfer rate for case 2.

axial step size is varied by two orders of magnitude, the numerical scheme is not only stable but the predicted heat-transfer results are also indistinguishable.

The computing times for these cases are summarized in Table 2 along with the grid sizes used. As can be seen, the coarsest grid (50-point with DXMAX = 10*Rn*) used took 16 s on a Cray Y/MP whereas the two finer grids (150-point with DXMAX = 1*Rn* and 50-point with DXMAX = 0.15*Rn*) took 498 s and 513 s, respectively. Clearly, some of the fine grids used in this case amount to an overkill; however, in this case they demonstrate an important issue: viz., that with the present three-dimensional PNS scheme the flowfield predictions are relatively insensitive to axial and axis-normal grid-refinement effects. Consequently, accurate flowfield predictions can be obtained with relatively coarse grids that require short computing times and are, thus, quite affordable. In fact, subsequent results will show these conclusions are also valid in general for other more complicated flow conditions.

Transitional/Turbulent Flow Conditions (Cases 2 and 3)

The case 2 transitional/turbulent conditions correspond to the Reentry-F flight altitude of 80,000 ft and 0.14-deg angle of attack conditions.[35,37] At this altitude the Mach number is 19.97 and the nose radius (*Rn*) is 0.14 in. The case 3 transitional/turbulent conditions correspond to the Reentry-F flight altitude of 65,000 ft and 0.715-deg angle-of-attack conditions.[35,37] The Mach number at this altitude is also 19.97, but the nose radius (*Rn*) is 0.151 in.

Figure 4 shows the PNS predictions using the Cebeci-Smith eddy-viscosity model and the Dhawan-Narasimha transition model. In this calculation, transition was initiated at an axial location of 566*Rn*, and a symmetric transition front was used, although the data indicated that the windward transition was initiated earlier. As shown in this figure, the agreement in the transitional/turbulent region is not very good (especially along the windward streamline). In their VSL study, Thompson et al.[37] ignored the windward heating rates; however, their predicted leeward heating rates are in close agreement with the PNS results shown in Fig. 4.

Since the angle of attack for this case is small, a zero angle-of-attack investigation of the turbulent and transition models used (Fig. 5) in this study was conducted. We considered the original Cebeci-Smith turbulence model with and without the scaling modifications suggested by Finson et al.[38] The original Cebeci-Smith model uses the local viscosity and density values in the Van Driest damping terms in the inner eddy viscosity. Finson et al.[38] suggested that using the wall viscosity and density values instead gave better agreement with their calculations using a higher order turbulence model. However, Fig. 5 shows that the modifications of Finson et al.[38] result in a substantial overprediction (40–50%) of the final turbulent heating rates. On the other hand, the original Cebeci-Smith model does a very good job of predicting the correct final turbulent heating levels.

The transition length predicted by the Dhawan-Narasimha model, however, substantially overpredicts the actual transi-

tion region. In this case, the Dhawan-Narasimha model predicts a more gradual transition to turbulence, with the flow only becoming fully turbulent at the body end. To see the effects of transition location, a calculation was also made using the original Cebeci-Smith model with instantaneous transition to fully turbulent conditions initiated at an axial location of $750Rn$. As can be seen from Fig. 5, in this case the predicted afterbody heating rates agree almost identically with the data. These results show that in this case the afterbody flow along the leeward streamline is probably fully turbulent by $x > 750Rn$, which is about 4 ft shorter than the predictions of the Dhawan-Narasimha model. For a 13-ft long body, this is a significant difference.

The most encouraging aspect of these calculations is that they show that under these hypersonic conditions the original Cebeci-Smith model (without pressure gradient effects) does an excellent job of predicting the correct turbulent levels, and the observed differences are primarily due to the modeling of the transition region. Encouraged by this, a final angle-of-attack calculation was made in which instantaneous transition to fully turbulent conditions was used with an asymmetric transition front. By looking at the data, the leeward transition was initiated at $x = 750Rn$, and the windward transition was initiated at $x = 525Rn$. The results of this calculation are shown in Fig. 6, and they show that the predictions along the windward and leeward streamlines are in very close agreement with the flight data.

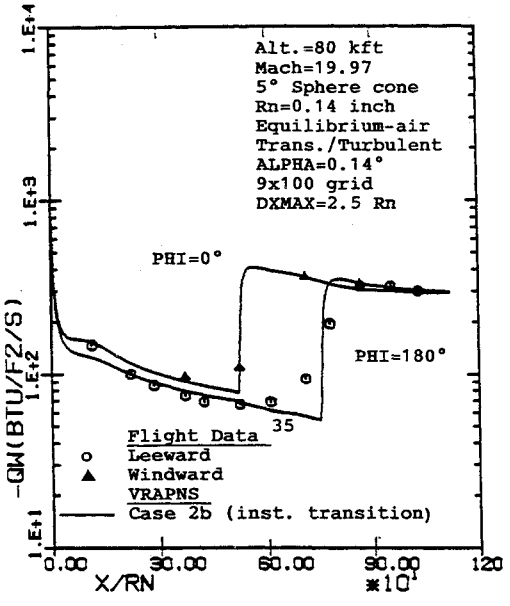

Fig. 6 Axial distribution of the wall heat-transfer rate for case 2 with an asymmetric transition front and instantaneous transition to turbulence.

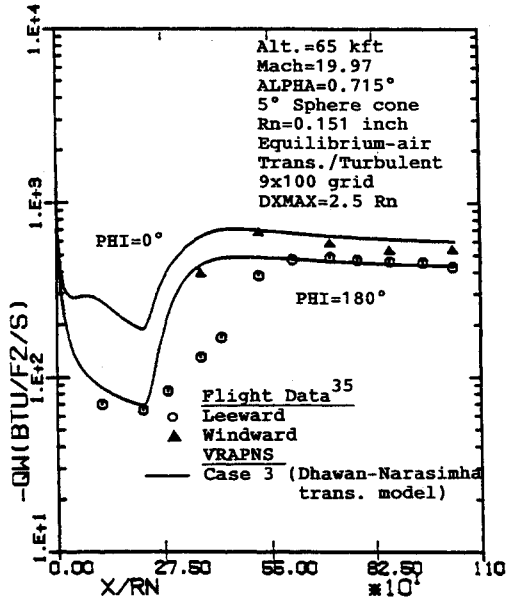

Fig. 7 Axial distribution of the wall heat-transfer rate for case 3 with Dhawan-Narasimha transition model.

The results of a PNS calculation at 65,000 ft (case 3) are shown in Fig. 7. In this case a single calculation was done using the Dhawan-Narasimha transition model with transition to turbulence initiated at $x = 263Rn$. In this case also the results show that the predictions in the fully turbulent afterbody region ($x > 600Rn$) are in close agreement with flight data along the windward and the leeward streamlines. However, in the transition region ($260Rn < x < 600Rn$), the Dhawan-Narasimha model underpredicts the transition length (especially along the leeward streamline). In short, these results show that the present numerical predictions in the laminar and fully turbulent regions are very reliable and in close agreement with the flight data. The original Cebeci-Smith model (without pressure gradient effects) does a very good job of predicting the proper turbulent heating levels. The predictions of the Dhawan-Narasimha transition model are, however, not accurate. It tends to significantly overpredict the transition length at higher altitudes and significantly underpredicts the transition lengths at lower altitudes.

The computing times and grids used for these calculations are also shown in Table 2. In general, these case 2 and case 3 calculations were done using 9 crossflow planes, 100 axis-normal points, and DXMAX = $2.5Rn$. The required computing times were between 4–5 min on a Cray Y/MP; however, a larger DXMAX (5–$10Rn$) could easily be used to substantially reduce the computing times without compromising accuracy.

12.84/7-Deg Straight and Bent-Bicone Calculations

The straight and bent-bicone configurations used in these comparisons were tested in the NASA Langley Expansion-Tube Facility.[36] Present numerical predictions have been compared with the available experimental data on the surface heat-transfer rates. The vehicle geometries are shown in Fig. 8, which corresponds to a 12.84/7-deg bicone with and without a 7-deg bent nose. The nose radius for these cases is 0.151 in., and the bodies are approximately $32Rn$ long. The freestream conditions for this case are given in Table 1 and correspond to

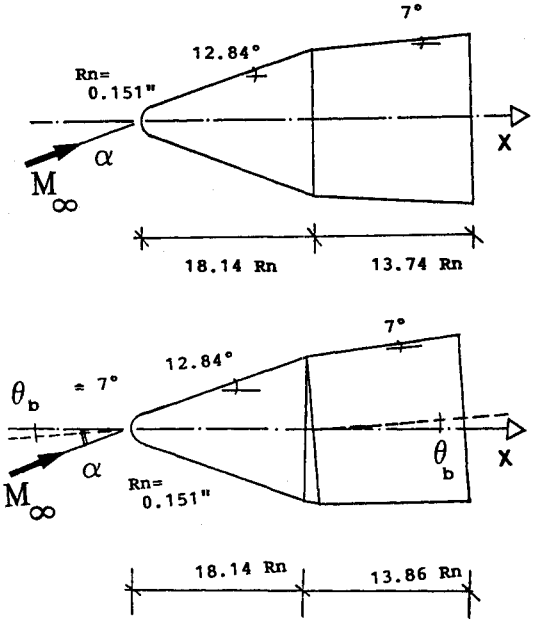

Fig. 8 12.84/7-deg straight and bent-bicone configurations.

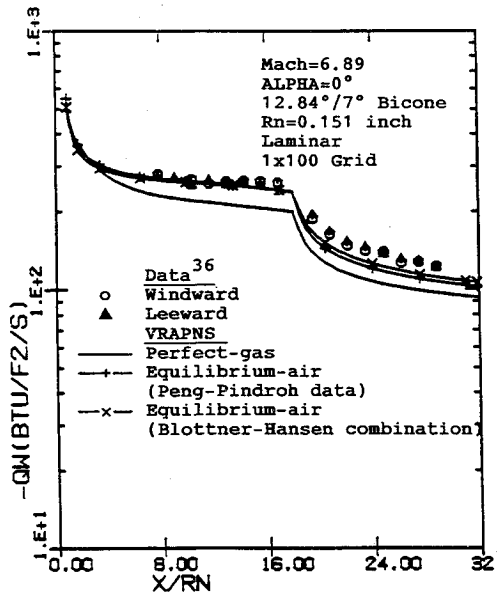

Fig. 9 Effects of gas model and equilibrium-air property data on the axial distribution of the wall heat-transfer rate for case 4.

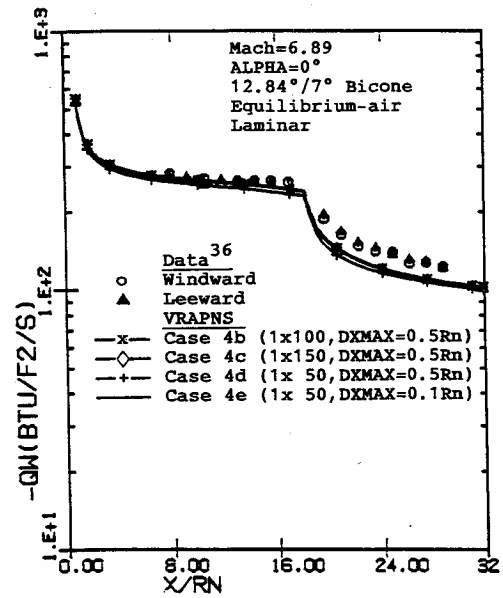

Fig. 10 Effects of axial and axis-normal grid refinement on the axial distribution of the wall heat-transfer rate for case 4.

Table 3 Computing times for cases 4–7 (Mach 6.89, laminar)

Case	Biconic geometry	AOA, deg[a]	Gas model[b]	DXMAX, *Rn*	Grid[c] N3 × N2 × N1	Time, s[d]
4a	Straight	0.0	PG	0.5	1 × 100 × 73 C	19
4b	Straight	0.0	EQ	0.5	1 × 100 × 73 C	20
4c	Straight	0.0	EQ	0.5	1 × 150 × 73 C	39
4d	Straight	0.0	EQ	0.5	1 × 50 × 73 C	7
4e	Straight	0.0	EQ	0.1	1 × 50 × 311 C	58
5a	Bent	7.0	EQ	0.5	33 × 50 × 73 C	92
5b	Bent	7.0	EQ	0.5	65 × 50 × 73 C	174
6a	Straight	20.	EQ	0.5	33 × 50 × 73 C	88
6b	Straight	20.	EQ	0.5	65 × 50 × 73 C	227
6c	Straight	20.	EQ	0.5	101 × 50 × 73 C	371
7a	Bent	27.	EQ	0.5	33 × 50 × 73 A	133
7b	Bent	27.	EQ	0.5	65 × 50 × 73 E	287
7c	Bent	27.	EQ	0.5	33 × 50 × 73 E	148

[a]AOA = angle of attack measured with respect to forecone axis.
[b]PG = Perfect-gas model, EQ = equilibrium-air gas model.
[c]N1, N2, and N3 are the number of grid points in the streamwise, axis-normal, and crossflow directions, respectively. The notations of A, C, and E mean algebraic, cylindrical, and elliptic grids, respectively.
[d]Computing times on Cray Y/MP with CFT77 compiler and autovectorization.

the Mach 6.89 flow at 0-, 7-, 20-, and 27-deg angle of attack with respect to the forecone axis. Fully laminar flow conditions were assumed and the gas model used was equilibrium-air.

The present PNS calculations are actually marched along the forebody axis. In short, the bent-nose configuration is treated as a sphere-cone configuration with a bent afterbody (a simple coordinate rotation). The angle of attack in the present computations is measured with respect to the forecone axis, whereas for the corresponding wind-tunnel tests[36] it was measured with respect to the aftcone axis. We feel that measuring the angle of attack with respect to the forecone axis is a better representation of the actual flow complexity because, for the bent-nose case, the forebody flowfield conditions are in fact much more severe than that indicated by the angle of attack with respect to the afterbody. Incidently, the experimental data were also obtained using the forebody axis as the reference axis,[36] and thus direct comparisons were possible without any ambiguity about gauge locations. The following sections show some results for the various calculations done using this straight and bent-nose configuration.

0-Deg Angle-of-Attack Bicone Calculations (Case 4)

Case 4 corresponds to the zero angle-of-attack flow over the 12.84/7-deg bicone. The effects of gas model and equilibrium-air transport property data are shown in Fig. 9. The results show that a perfect-gas model underpredicts the surface heating rates by 25–30%. The predictions of the equilibrium-air gas model are in good agreement with the experimental data. According to Miller et al.,[36] the uncertainty in the heat-transfer data is about ± 15%. In the forecone region, the equilibrium-air predictions and the data are in excellent agreement. In the aftcone region, the predictions are approximately 10% lower than the data, but within the data uncertainty. The present predictions agree with the computational results of Miller et al.[36] in being on the lower side, but the overall agreement is better. This figure also shows that the predictions using Peng and Pindroh[26] transport property data and the Blottner-Hansen combination are almost identical in the forecone region and within a few percent of each other in the aftcone region. However, there is general consensus that the Peng and Pindroh[26] data are more accurate and will be used in the remaining calculations.

The effects of axis-normal and axial grid refinement are shown in Fig. 10. The results using DXMAX of $0.5Rn$ and $0.1Rn$ show no differences and show that DXMAX = $0.5Rn$ is an adequate choice to resolve various geometry and flowfield features. The axis-normal grid refinement shows no difference between the 100-point and 150-point grids, whereas the 50-

point grid predicts 2–5% lower heat-transfer rates in some regions. In view of these grid refinement studies, it was decided that a 50-point grid between the body and the shock along with DXMAX = 0.5*Rn* will be quite adequate for these calculations as well as the subsequent angle-of-attack calculations. The computing times and the grids used for these case 4 calculations (Table 3) show that increasing the grid size causes an almost proportional increase in the overall computing times.

7-Deg Angle-of-Attack Bent-Bicone Calculations (Case 5)

Case 5 corresponds to the bent-bicone configuration at 7-deg angle of attack. Figure 11 shows the axial distributions of the wall heat-transfer rate along the windward and leeward streamlines for this case. In this case, there is very good agreement between the predictions and the data along the windward streamline, whereas the heating rates along the leeward streamline differ by 10–20%. However, in view of the 15% data uncertainty, this agreement is also quite good. According to Miller et al.,[36] the measured fluctuations and associated data uncertainty along the leeward streamline were more than that on the windward side. In this figure, results are shown for two cylindrical grids using 33 and 65 crossflow planes with equal angular spacing. The corresponding crossflow distribution of wall heat-transfer rate at $x = 29.5Rn$ is shown in Fig. 12. These figures show that the predictions of the two grids considered are almost identical except for a small 1–2% difference on the leeside in the aftcone region. In short, the flowfield predictions for this case appear to be independent of further crossflow grid refinement. The adequacy of the axial and axis-normal grids used have already been established from the case 4 calculations (Fig. 10).

The Y/MP computing times and grids used for these case 5 calculations are also shown in Table 3. These times also show that, in general, changing the grid size in any of the three axial, axis-normal, and crossflow directions has almost a proportional effect on the final computing times.

20-Deg Angle-of-Attack Bicone Calculations (Case 6)

The 20-deg angle-of-attack results for the straight bicone conditions are shown in Figs. 13 and 14. These calculations

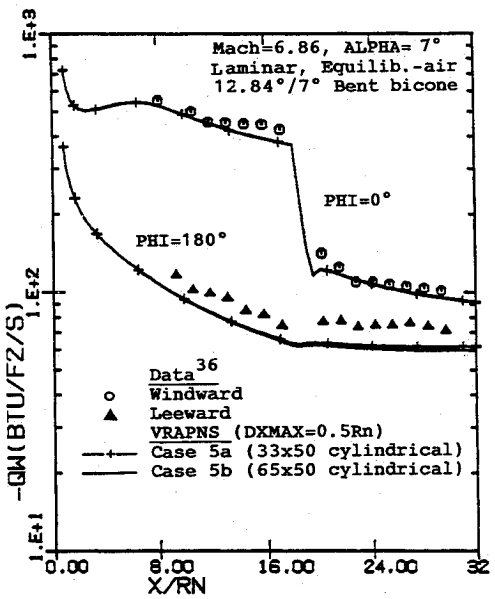

Fig. 11 Axial distribution of the wall heat-transfer rate for case 5.

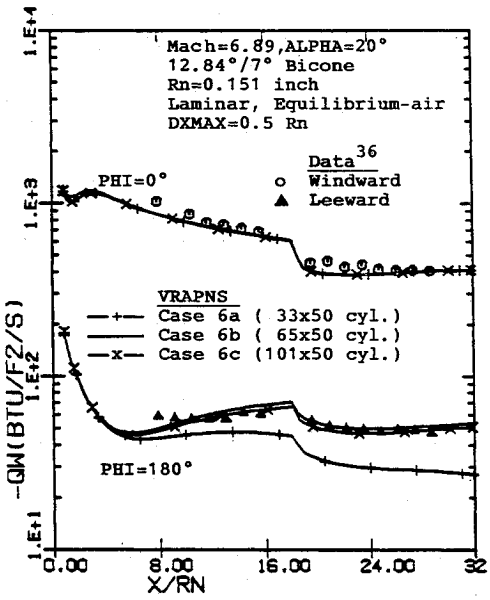

Fig. 13 Axial distribution of the wall heat-transfer rate for case 6.

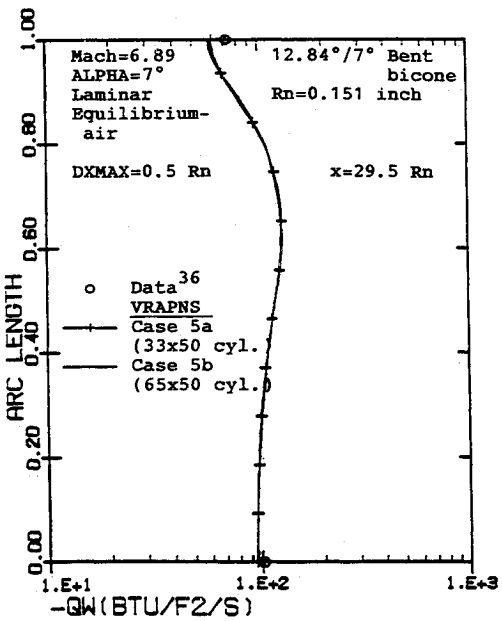

Fig. 12 Crossflow distribution of the wall heat-transfer rate for case 5 at $x = 29.5Rn$.

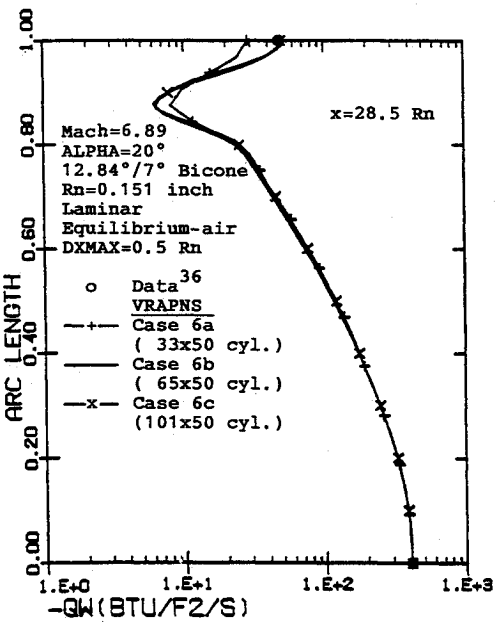

Fig. 14 Crossflow distribution of the wall heat-transfer rate for case 6 at $x = 28.5Rn$.

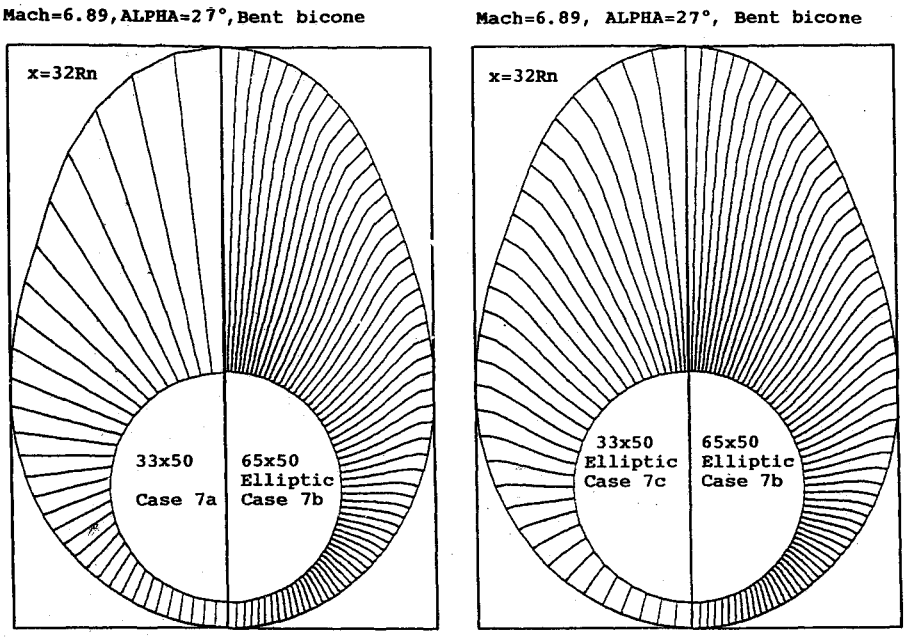

Fig. 15 Comparison of the ξ_3 = const coordinate lines at $x = 32Rn$ for the various case 7 grids.

(along with the following bent-bicone calculations) bring forth some very important aspects of the leeside flowfield under large angle-of-attack conditions when crossflow separation exists on the leeside. Miller et al.[36] noted from their experimental data that as the angle of attack was increased, the leeward heating rates toward the body end first decreased (as expected) but then increased quite significantly with increasing angle of attack. This trend of the heating rate was even more accentuated for the bent-bicone case. Miller et al.[36] investigated this effect and closely related it to the formation of crossflow separation and associated longitudinal vortices on the leeside under large angle-of-attack conditions. From a computational point of view this means that if this interaction between the longitudinal vortices on the leeside and the leeward wall heating rates is indeed correct, it will be essential to adequately resolve this crossflow separated region to accurately predict the leeward heating rates under large angle-of-attack conditions. The following numerical results do indeed confirm this conclusion.

The axial distribution of the windward and leeward wall heat-transfer rates for the straight bicone at 20-deg angle-of-attack conditions (case 6) are shown in Fig. 13, and the corresponding crossflow distribution at $x = 28.5Rn$ is shown in Fig. 14. Results are shown for three uniformly spaced cylindrical grids using 33, 65, and 101 crossflow planes, respectively. Figure 13 shows that the crossflow grid refinement has almost no impact on the predicted windward heating rates, which are in very good agreement with the data. The leeward heating rates are, however, significantly affected by the crossflow grid refinement. The leeward surface heating rates predicted by the coarse (33 crossflow plane) grid are as much as 70% lower than the data. However, the finer grid (64 and 101 crossflow plane) results are in excellent agreement with the data. As seen from Fig. 14, the predictions of the three grids are almost identical until the start of the crossflow separated region. In general, the wall heat-transfer rate initially decreases as we move from the windward to the leeward pitch plane, reaches a minimum at the onset of crossflow separation, and then rapidly increases toward the leeward pitch plane. The 33-plane grid does not adequately resolve the crossflow separated region and, thus, underpredicts this increase in leeward wall heat-transfer rate. The 64-plane and the 101-plane grids have the leeward grid resolution needed to accurately predict the crossflow separated region and the associated wall heat-transfer rate. Figure 14 further shows that a uniform crossflow grid refinement is really not required for improved accuracy, rather only a refinement of leeside grid can be done. This understanding of the required grid resolution is used for the following 27-deg angle-of-attack bent-bicone calculations where it is shown that, with an appropriate handling of the computational grid, accurate results can even be obtained with a 33-plane grid. The computing times for the these case 6 calculations are shown in Table 3.

27-Deg Angle-of-Attack Bent-Bicone Calculations (Case 7)

Figure 15 shows the three computational grids used for the bent-bicone calculations at 27-deg angle of attack (case 7). These grids consist of a uniformly spaced algebraic grid with 33 crossflow planes, a 64-plane elliptic grid with nonuniform grid spacing, and a 33-plane elliptic grid with nonuniform grid spacing. The 64-plane and 33-plane elliptic grids (Fig. 15) are such that the leeward grid size is equivalent to a uniformally spaced 129-plane cylindrical grid. The advantage of using an elliptic grid is to be able to use different grid clustering schemes at the body and at the shock. With cylindrical grids, especially at large angles of attack, nonuniform crossflow grid clustering can lead to an undesirable crossflow grid distribution at the bow shock. With the elliptic grid-generation scheme, a uniform or near-uniform crossflow grid spacing can be maintained at the shock, while using very clustered crossflow grids at the body (see Fig. 15).

The axial and crossflow distributions of wall heat-transfer rate for the bent-bicone at 27-deg angle of attack (case 7) are shown in Figs. 16 and 17, respectively. The axial distributions of the wall heat-transfer rate (Fig. 16) show that along the windward streamline the predictions of the three grids are in excellent agreement with each other and also with the experimental data. Along the leeward streamline, however, the predictions of the uniformly spaced 33-plane algebraic grid underpredict the data by as much as 140%. On the other hand, the nonuniform 64-plane and 33-plane elliptic grids are in close agreement with the data along the leeward as well as the windward streamlines, with maximum differences within the limits of data uncertainty.

The crossflow distribution of the wall heat-transfer rate at $x = 29.5Rn$ (Fig. 17) shows that (as expected) the predictions of the three grids are in excellent agreement until the onset of crossflow separation. The crossflow separated region on the leeside predicted using the nonuniform 64-plane grid is shown in Fig. 18. As can be seen from this figure, under these

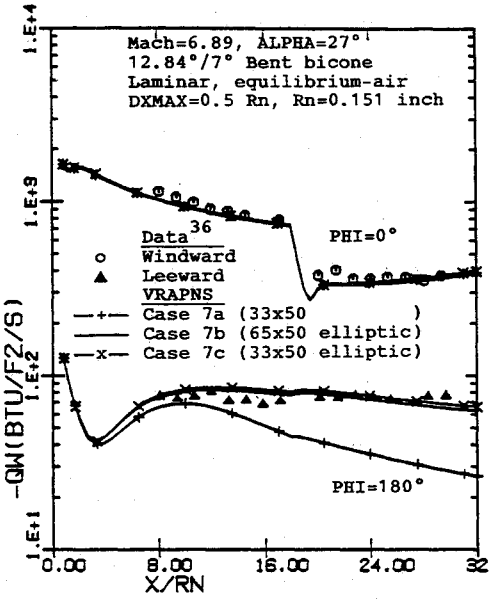

Fig. 16 Axial distribution of the wall heat-transfer rate for case 7.

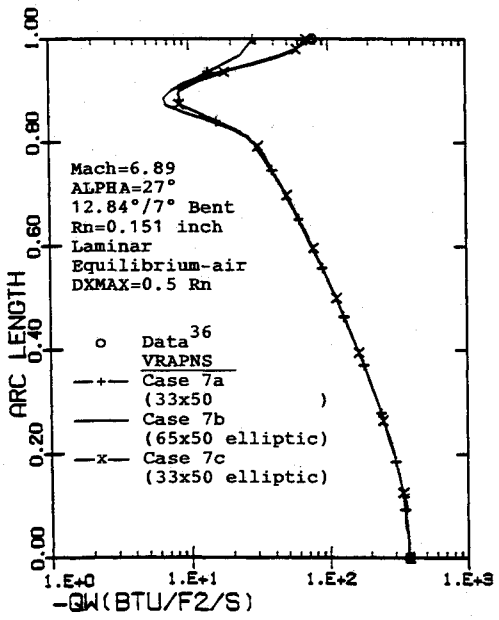

Fig. 17 Crossflow distribution of the wall heat-transfer rate for case 7 at $x = 29.5Rn$.

conditions, the leeside has a well-defined crossflow recirculation region with a well-defined vortical eye near the leeward pitch plane. This clearly confirms the reasoning used by Miller et al.[36] to explain the experimentally observed trends of the leeward heating rates.

The computing times for the various case 7 calculations are also shown in Table 3 along with the corresponding grid sizes. These results show that while providing similar solution accuracy, the nonuniform 33-plane elliptic grid for the bent-bicone case took about half as long to do than the 64-plane elliptic grid. In this case, the 33-plane elliptic grid took only 11% longer to do than the corresponding 33-plane algebraic grid. When compared with the enhanced computational flexibility and solution accuracy provided by the elliptic grid generation scheme, this difference is simply insignificant.

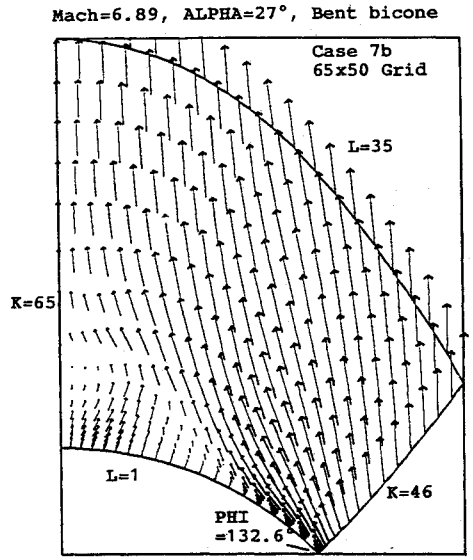

Fig. 18 Details of the leeside crossflow separated region for case 7 at $x = 32Rn$.

Conclusions

A new three-dimensional perfect-gas and equilibrium-air PNS scheme has been developed to study three-dimensional hypersonic flows over complex three-dimensional configurations. This PNS scheme has been used to study the flow over various conical configurations over a Mach number range of 6.89–20 and an angle-of-attack range of 0–27 deg. Comparisons are made with available flight and wind-tunnel data in terms of the surface heat-transfer rate. The results of this study substantiate the following comments:

1) A new three-dimensional PNS scheme has been developed to study perfect-gas and equilibrium-air hypersonic flows over three-dimensional configurations. This three-dimensional PNS scheme is unconditionally time-like in the subsonic as well as the supersonic flow regions and does not require the use of any sublayer approximation.

2) This PNS scheme uses a fourth-order accurate crossflow and axis-normal smoothing approach and a second-order accurate streamwise smoothing approach and has the robustness of being able to use a wide range of coarse to fine grids in all three coordinate directions. This results in accurate wall heat-transfer and skin-friction predictions even with coarse computational grids. The numerical scheme is stable and accurate over a wide range of small-to-large axial step sizes (even when the step size variations involve a change of two orders of magnitude).

3) Comparisons with the Reentry-F flight data show excellent agreement under laminar and fully turbulent conditions using the Cebeci-Smith turbulence model. The predictions of the transition model of Dhawan and Narasimha, however, do not agree well with the flight data.

4) Large angle-of-attack calculations on 12.84/7-deg biconic and bent-biconic configurations show that proper resolution of the leeside crossflow separated flow region is essential for accurately predicting the leeward heating rates. With a proper griding approach, very good agreement is achieved with available experimental data from the NASA Langley Expansion Tunnel.

5) In general, it is seen that for the various configurations tested, the numerical predictions are either in excellent agreement with available data or at worse within the uncertainty bounds of the data.

Acknowledgments

The work reported in this paper was supported in part by the NASA Lewis Research Center under Contract NAS3-25450. The encouragement and cooperation provided by the

contract monitor Tom Benson, Louis Povinelli, and Dan Whipple during the course of this effort are gratefully acknowledged. The authors would also like to thank James Daywitt and Darius N. Brant of GE Reentry Systems Department, Philadelphia, Pennsylvania, for their valuable suggestions and help in obtaining the Reentry-F flight data.

References

[1]Richardson, P., Parlette, E., Morrison, J., and Switzer, G., "Heat Transfer and Pressure Comparisons Between Computation and Wind Tunnel for Research Hypersonic Aircraft," AIAA Paper 89-0029, Jan. 1989.

[2]Rudy, D., Thomas, J., Kumar, A., and Gnoffo, P., "A Validation Study of Four Navier-Stokes Codes for High-Speed Flows," AIAA Paper 89-1838, June 1989.

[3]Thomas, P. D., and Neier, K. L., "Navier-Stokes Simulation of Three-Dimensional Hypersonic Equilibrium Flows with Ablation," *Journal of Spacecraft and Rockets,* Vol. 27, No. 2, March–April 1990, pp. 143–149.

[4]Murray, A. L., and Lewis, C. H., "Hypersonic Three-Dimensional Viscous Shock-Layer Flows over Blunt Bodies,"*AIAA Journal,* Vol. 16, No. 12, Dec. 1978, pp. 1279–1286.

[5]Thareja, R. R., Szema, K. Y., and Lewis, C. H., "Chemical Equilibrium Laminar or Turbulent Three-Dimensional Viscous Shock-Layer Flows," *Journal of Spacecraft and Rockets,* Vol. 20, No. 5, Sept.–Oct. 1983, pp. 454–460.

[6]Kim, M. D., Bhutta, B. A., and Lewis, C. H., "Three-Dimensional Effects upon Real Gas Flows Past the Space Shuttle," AIAA Paper 84-0225, Jan. 1984.

[7]Bhutta, B. A., and Lewis, C. H., "An Implicit Parabolized Navier-Stokes Scheme for High-Altitude Reentry Flows," AIAA Paper 85-0036, Jan. 1985.

[8]Bhutta, B. A., Lewis, C. H., and Kautz, F. A., II, "A Fast Fully-Iterative Parabolized Navier-Stokes Scheme for Chemically-Reacting Reentry Flows," AIAA Paper 85-0926, June 1985.

[9]Bhutta, B. A., and Lewis, C. H., "Prediction of Three-Dimensional Hypersonic Flows Using a Parabolized Navier-Stokes Scheme," *Journal of Spacecraft and Rockets,* Vol. 26, No. 1, Jan.–Feb. 1989, pp. 4–13; see also AIAA Paper 85-1604, June 1985.

[10]Bhutta, B. A., and Lewis, C. H., "Prediction of Axisymmetric Hypersonic Blunt-Body Flows Using a Parabolized Navier-Stokes Scheme," AIAA Paper 89-1831, June 1989.

[11]Bhutta, B. A., and Lewis, C. H., "PNS Predictions of Three-Dimensional Hypersonic Flows with Strong Crossflow Effects," *Journal of Thermophysics and Heat Transfer,* Vol. 4, Jan. 1990, pp. 27–36; see also AIAA Paper 88-2696, June 1988.

[12]Bhutta, B. A., and Lewis, C. H., "Three-Dimensional Hypersonic Nonequilibrium Flows at Large Angles of Attack," *Journal of Spacecraft and Rockets,* Vol. 26, No. 3, May–June 1989, pp. 158–166; see also AIAA Paper 88-2568, June 1988.

[13]Bhutta, B. A., and Lewis, C. H., "Large Angle-of-Attack Viscous Hypersonic Flows Over Complex Lifting Configurations," *Journal of Spacecraft and Rockets,* Vol. 27, No. 2, March–April 1990, pp. 194–204; see also AIAA Paper 89-0269, Jan. 1989.

[14]Bhutta, B. A., and Lewis, C. H., "Prediction of Nonequilibrium Viscous Hypersonic Flows Over Lifting Configurations," AIAA Paper 89-1696, June 1989.

[15]Lubard, S. C., and Helliwell, W. S., "Calculation of the Flow on a Cone at High Angle of Attack," R & D Associates, Santa Monica, CA, Rept. RDA-TR-150, Feb. 1973.

[16]Helliwell, W. S., Dickinson, R. P., and Lubard, S. C., "Viscous Flows Over Arbitrary Geometries at High Angle of Attack," AIAA Paper 80-0064, Jan. 1980.

[17]Schiff, L. B., and Steger, J. L., "Numerical Simulation of Steady Supersonic Viscous Flows," AIAA Paper 79-0130, Jan. 1979.

[18]Kaul, U. K., and Chaussee, D. S., "AFWAL Parabolized Navier-Stokes Coded: 1983 AFWAL/NASA Merged Baseline Version," Air Force Flight Dynamics Laboratory, Wright Patterson AFB, OH, AFWAL-TR-83-3118, Oct. 1983.

[19]Shanks, S. P., Srinivasan, G. R., and Nicolet, W. E., "AFWAL Parabolized Navier-Stokes Code: Formulation and User's-Manual," Air Force Flight Dynamics Laboratory, Wright Patterson AFB, OH, AFWAL-TR-823034, June 1979.

[20]Vigneron, Y. C., Rakich, J. V., and Tannehill, J. C., "Calculations of Supersonic Viscous Flows Over Delta Wings with Sharp Subsonic Leading Edges," AIAA Paper 78-1137, July 1978.

[21]Stalnaker, J. F., Nicholson, L. A., Hanline, D. S., and McGraw, E. H., "Improvements to the AFWAL Parabolized Navier-Stokes Code Formulation," Air Force Flight Dynamics Laboratory, Wright Patterson AFB, OH, AFWAL-TR-86-3076, Sept. 1986.

[22]Viviand, H., "Conservative Forms of Gas Dynamics Equations," *La Recherche Aerospatiale,* Vol. 1, Jan.–Feb. 1974, pp. 65–68.

[23]Peyert, R., and Viviand, H., "Computations of Viscous Compressible Flows Based on the Navier-Stokes Equations," AGARD-AG-212, Sept. 1975.

[24]White, F. M., *Viscous Fluid Flow,* McGraw-Hill, New York, NY, 1974.

[25]Miner, E. W., Anderson, E. C., and Lewis, C. H., "A Computer Program for Two-Dimensional and Axisymmetric Nonreacting Perfect Gas and Equilibrium Chemically Reacting Laminar, Transitional and-or Turbulent Boundary-Layer Flows," NASA CR-132601, May 1975.

[26]Peng, T. C., and Pindroh, A. L., "An Improved Calculation of Gas Properties at High Temperature Air," Aerospace Division, The Boeing Co., Seattle, WA, Boeing Rept. D2-11722, 1962.

[27]Blottner, F. G., Johnson, M., and Ellis, M., "Chemically Reacting Viscous Flow Program for Multi-Component Gas Mixtures," Sandia Laboratories, Albuquerque, NM, Rept. SC-RR-70-754, Dec. 1971.

[28]Hansen, F. C., "Approximations for the Thermodynamic and Transport Properties of High-Temperature Air," NASA TR R-50, 1959.

[29]Chaussee, D. S., Patterson, J. L., Kutler, P., Pulliam, T. H., and Steger, J. L., "A Numerical Simulation for Hypersonic Viscous Flows Over Arbitrary Geometries at High Angle of Attack," AIAA Paper 81-0050, Jan. 1981.

[30]Sorenson, R. L., and Steger, J. L., "Simplified Clustering of Nonorthogonal Grids Generated by Elliptic Partial Differential Equations," NASA TM-73252, Aug. 1977.

[31]Chaussee, D. S., and Steger, J. L., "Three Dimensional Viscous Flowfield Program; Part 2; A Curvilinear Grid and Body Generation Program for Generalized Configurations (Interim Report)," Flow Simulations, Inc., Sunnyvale, CA, AFWAL-TM-81-64-FIMG, March 1981.

[32]Kaul, U. K., and Chaussee, D. S., "A Comparative Study of the Parabolized Navier-Stokes (PNS) Code Using Various Grid Generation Techniques," AIAA Paper 84-0459, Jan. 1984.

[33]Cebeci, T., and Smith, A. M. O., *Analysis of Turbulent Boundary Layers,* Academic Press, New York, NY, 1974.

[34]Dhawan, S., and Narasimha, R., "Some Properties of Boundary Layer Flow During the Transition from Laminar to Turbulent Motion," *Journal of Fluid Mechanics,* Vol. 3, Jan. 1958, pp. 418–436.

[35]Stainback, P. C., Johnson, C. B., Boney, L. B., and Wicker, K. C., "Comparison of Theoretical Predictions and Heat-Transfer Measurements for a Flight Experiment at Mach 20 (Reentry F)," NASA TM X-2560, July 1972.

[36]Miller, C. G., III, Micol, J. R., and Gnoffo, P. A., "Laminar Heat-Transfer Distribution on Biconics at Incidence in Hypersonic-Hypervelocity Flows," NASA TP-2213, Jan. 1985.

[37]Thompson, R. A., Zoby, E. V., Wurster, K. E., and Gnoffo, P. A., "An Aerothermodynamic Study of Slender Conical Vehicles," AIAA Paper 87-1475, June 1987.

[38]Finson, M. L., Ameer, P. G., Person, J. C., Cronin, J. F., and Parker, P. D., "Non-Equilibrium Boundary-Layer Code; Volume I of II, Numerical Methodology; Volume II of II, User's Manual," Physical Sciences Inc., Dascomb Research Park, Andover, MA, PSI-9030/TR-676, June 1988.

Ernest V. Zoby
Associate Editor